

Tunneling dynamics of ^{164}Dy supersolids and droplets


S. I. Mistakidis^{1,2,3}, K. Mukherjee⁴, S. M. Reimann⁴ and H. R. Sadeghpour²

¹*Department of Physics, Missouri University of Science and Technology, Rolla, Missouri 65409, USA*

²*ITAMP, Center for Astrophysics | Harvard and Smithsonian, Cambridge, Massachusetts 02138 USA*

³*Department of Physics, Harvard University, Cambridge, Massachusetts 02138, USA*

⁴*Mathematical Physics and NanoLund, Lund University, Box 118, 22100 Lund, Sweden*

 (Received 8 January 2024; revised 6 June 2024; accepted 21 June 2024; published 25 July 2024)

The tunneling dynamics of a magnetic ^{164}Dy quantum gas in an elongated or pancake skewed double-well trap is investigated with a time-dependent extended Gross-Pitaevskii approach. Upon lifting the energy offset, different tunneling regimes can be identified. In the elongated trap and for sufficiently large offset, the different configurations exhibit collective macroscopic tunneling. For smaller offset, partial reflection from and transmission through the barrier lead to density accumulation in both wells, and eventually to tunneling locking. One can also reach the macroscopic self-trapping regime for increasing relative dipolar interaction strength, while tunneling vanishes for large barrier heights. A richer dynamical behavior is observed for the pancake-like trap. For instance, the supersolid maintains its shape, while the superfluid density gets distorted, signifying the emergence of peculiar excitation patterns in the macroscopic tunneling regime. The findings reported here may offer alternative ways to probe distinctive dynamical features in the supersolid and droplet regimes.

DOI: [10.1103/PhysRevA.110.013323](https://doi.org/10.1103/PhysRevA.110.013323)

I. INTRODUCTION

Dipolar Bose-Einstein condensates (dBECs) consisting of magnetic chromium [1] or lanthanides such as dysprosium [2], erbium [3], and europium [4] offer highly flexible platforms to unravel exotic many-body phases of matter (for reviews, see Refs. [5–7]). The interplay of long-range anisotropic dipole-dipole interactions (DDI), short-range isotropic interactions, and quantum fluctuation contributions may prevent a collapse of the dBEC [8–13]. It gives rise to the (by now well-studied) supersolid (SS) and droplet phases, see the recent review of Ref. [7].

Advances in ultracold atoms have opened up new possibilities to observe this intricate SS state of matter. Predictions were made for Rydberg-excited BECs [14] and in the dipole-blockade regime [15]. Early experimental realizations of supersolidity were reported, for example, in spin orbit [16] and BECs coupled to optical cavities [17,18]. The above-mentioned dBECs, however, provide a particularly favorable setting since the localization is not externally initiated, but rather is an intrinsic property resulting from the spontaneous symmetry breaking due to the interactions. Only shortly after the discovery of dipolar droplets, the SS state was uncovered in three milestone experiments with highly magnetic dysprosium and erbium atoms [19–21].

In dBECs, for the SS and self-bound states, quantum fluctuations play a major role. Similar to the description of stable self-bound droplets in binary BECs [22], they are commonly modeled with the extended Gross-Pitaevskii method (eGPE) [10,12,13,23,24], including the Lee-Huang-Yang (LHY) correction [25,26] to approximate quantum fluctuations to first order. In a dipolar SS, the spontaneous breaking of translational symmetry [19–21,27] gives rise to density modulations while partially retaining superfluid (SF) properties and exhibits both diagonal and off-diagonal

long-range order [28–33]. This phenomenon is underpinned by the presence of a roton minimum in the energy-momentum dispersion relation which has been experimentally probed [34–36]. Notably, in cases where long-range interactions are dominant, the dilute SF background density, characteristic of the SS phase, may vanish leading to the formation of isolated droplet lattice (DL) configurations [9,10,19].

SS and DL phases have been realized in elongated traps, where they can order periodically along one spatial dimension [19–21,37], and more recently, in planar droplet arrays in two dimensions [27,38,39]. In oblate trap geometries, states of dysprosium with different ground-state morphologies were predicted, from honeycomb to triangular, striped, and ring-shaped lattices [40–42]. In the presence of an optical lattice, a geometrical frustration of the dipolar droplet lattice may be induced, and more complicated phase patterns emerge [43]. Dipolar mixtures have more recently been investigated [44–47], for which alternating-domain supersolids have also been found [48]. Dynamical properties offer intriguing future prospects [49], and notable examples include (but are not limited to) interaction quenches [19,20,50,51], the formation of vortex configurations [52–54], the manifestation of persistent currents [55,56], or the impact of relevant thermal effects [39,57,58].

For BECs with short-range interactions, the tunneling dynamics in double-well potentials has been widely investigated, see, for instance, the review in Ref. [59] or the collected articles in Ref. [60]. Such systems constitute atomic analogues of the well-known superconducting Josephson junction [61] and exhibit tunneling phenomena [59,62] including, for instance, Josephson oscillations [63] and macroscopic quantum self-trapping [64]. However, the tunneling dynamics of dBECs in the SS and DL phases, and in particular, the interplay of short- and long-range interactions on the emergent tunneling

regimes remain largely unexplored. Additionally, since the droplet crystal configuration depends on the spatial dimension of the system, it would be intriguing to explore the impact of dimensionality on the emergent tunneling behavior. Relevant open questions, for instance, include whether the crystal arrangement retains its symmetry in the course of tunneling and how suppression of the latter occurs due to interactions in various dimensions.

Here, we report an attempt to theoretically investigate the tunneling dynamics of a dipolar SS or DL in a double-well potential within the eGPE framework. The approach is anticipated to capture the basic dBEC tunneling dynamics, while higher-order effects, such as additional tunneling channels or interband contributions, require more sophisticated approaches [65] and are left for future work.

The dBEC is initially confined in a tilted double-well potential, with the individual wells chosen to be elongated or pancake-like. Then the system is suddenly quenched from an initial energy offset between the wells to a symmetric double-well potential. The initial energy offset, the relative dipolar strength (i.e., contact versus dipolar coupling), and the barrier height determine the tunneling characteristics of the system. Prior to the quench, the single-well configurations exhibit the well-known formation of SF, SS, and DL states (see, e.g., the review of Ref. [7]). For an elongated double-well with a sufficiently large initial energy offset, the different dBEC configurations exhibit periodic oscillations between the wells with constant amplitude and frequency, thus featuring collective tunneling. When the offset is reduced, partial reflection and transmission occur through the barrier, resulting in the accumulation of density in both wells and eventually leading to tunnel locking. At long evolution times, in the self-bound DL regime, a significant population difference is established, distinguishing it from the SF phase where the imbalance vanishes. Additionally, the SS and DL states exhibit a reduced center-of-mass velocity compared to the SF phase, indicating their rigidity. Increasing the barrier height while keeping all other parameters fixed, it is possible to enter the macroscopic self-trapping regime. The different patterns also manifest in pancake-like double-well systems, however, with a richer phenomenology.

This paper proceeds as follows. Section II introduces the dBEC setting and the relevant eGPE framework. The ground-state phases of the system confined in a double-well with an energy offset for varying interactions are discussed in Sec. III. Consecutively, the resultant tunneling dynamics of the different phases after suddenly switching off the underlying energy offset is analyzed for an elongated double-well in Sec. IV and a pancake-like one in Sec. V. We summarize and comment on future perspectives in Sec. VI. In Appendix A, we discuss the effect of three-body recombination on the tunneling behavior, while Appendix B explicates the persistence of tunneling after a linear ramp of the energy offset. Appendix C further elaborates on some technical details.

II. EXTENDED GROSS-PITAEVSKII FOR THE DIPOLAR GAS

We consider a dBEC of ^{164}Dy atoms having a magnetic dipole moment $\mu_m = 9.93\mu_B$ (where μ_B is the Bohr

magneton) being polarized along the z direction. At zero temperature, the dynamics of the dBEC is modeled by the eGPE [10,12,13,23,24] containing the first-order LHY beyond mean-field correction

$$i\hbar \frac{\partial \psi(\mathbf{r}, t)}{\partial t} = \left[-\frac{\hbar^2}{2m} \nabla^2 + V(\mathbf{r}) + \frac{4\pi \hbar^2 a_s}{m} |\psi(\mathbf{r}, t)|^2 + \gamma(\epsilon_{dd}) |\psi(\mathbf{r}, t)|^3 + \int dr' U_{dd}(\mathbf{r} - \mathbf{r}') |\psi(\mathbf{r}', t)|^2 \right] \psi(\mathbf{r}, t). \quad (1)$$

The three-dimensional (3D) wave function is represented by $\psi(\mathbf{r}, t)$ and m is the mass of Dy atom. The long-range anisotropic DDI is $U_{dd}(\mathbf{r}, t) = \frac{\mu_0 \mu_m^2}{4\pi} \frac{1-3\cos^2\theta}{r^3}$. The angle between the relative distance \mathbf{r} of two dipoles and the z axis of the quantization axis (defined by the magnetic field) is denoted by θ , and μ_0 represents the permeability of the vacuum. Moreover, the dipolar atoms experience short-range contact interactions whose strength is quantified via the 3D s -wave scattering length, a_s , that can be experimentally tuned through Fano-Feshbach resonances [66,67]. The LHY term [25] approximates the lowest-order quantum fluctuation contributions to the energy functional. These fluctuations in three dimensions appear to be repulsive and scale with the gas density as $\sim n^{3/2}$, taking the form $\gamma(\epsilon_{dd}) = \frac{32}{3} g \sqrt{\frac{a_s^3}{\pi}} (1 + \frac{3}{2} \epsilon_{dd}^2)$ [26]. Its contribution is crucial for the system to sustain many-body self-bound states such as droplets and SS and it has been shown to adequately describe experimental observations (as reviewed in Ref. [7]).

In a 3D harmonic trap the relative strength $\epsilon_{dd} = a_{dd}/a_s$ between the DDI and the short-range interactions determines the many-body phase of the system [9]. In particular, the dipolar length of ^{164}Dy atoms is $a_{dd} = \mu_0 \mu_m^2 m / 12\pi \hbar^2 = 131a_B$, with a_B being the Bohr radius. For sufficiently small values of ϵ_{dd} , the system exhibits a SF phase. The equilibrium solution is determined by the delicate balance between the attractive or repulsive long-range dipolar interaction and the repulsive contact interaction. As the short-range scattering length decreases, the relative strength of the long-range dipolar interaction becomes dominant. Within a small range of ϵ_{dd} , the system favors the SS phase, where a periodic structure of localized densities coherently connected by a dilute superfluid background emerges. However, a further increase in ϵ_{dd} leads to a DL phase.

The initial state is prepared in an external 3D tilted double-well potential

$$V(\mathbf{r}) = \frac{1}{2} m (\omega_x^2 x^2 + \omega_y^2 y^2 + \omega_z^2 z^2) + V_D e^{-\frac{x^2}{2w^2}} + Dx, \quad (2)$$

where V_D is the barrier height and w is the barrier width. For our purposes, we use $V_D = 10 \hbar \omega_x$ and $w = 0.5 l_{\text{osc}}$, with $l_{\text{osc}} = \sqrt{\hbar / (m \omega_x)}$ being the harmonic oscillator length and ω_x denoting the frequency of the external confinement. The last term is the linear external field gradient of strength D that energetically favors the population on the left well. The tilt strength ranges from $D = 1 \hbar \omega_x / l_{\text{osc}}$ to $D = 10 \hbar \omega_x / l_{\text{osc}}$.

Our analysis extends from (i) an elongated double-well characterized by $(\omega_x, \omega_y, \omega_z) = 2\pi \times (19, 53, 81)$ Hz (with the single wells being similar to those in Refs. [19,37])

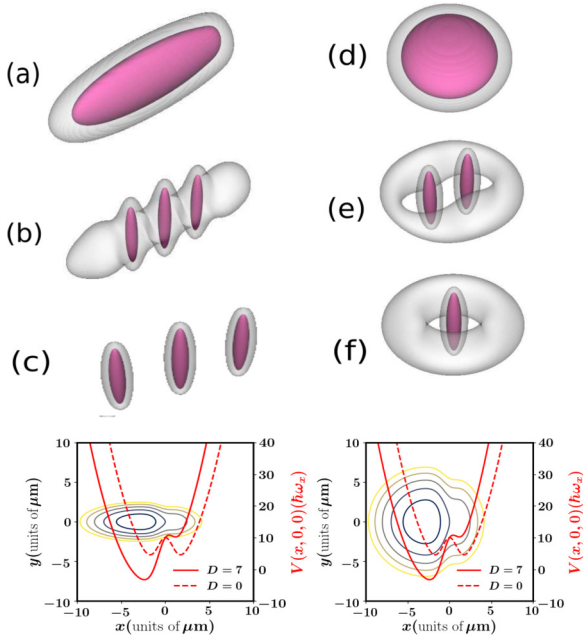


FIG. 1. Ground-state density isosurfaces of a dBEC initially localized on the left side of (a)–(c) an elongated and (d)–(f) pancake-like tilted double-well trap, as depicted by the contour lines in the lowest panels. The density isosurfaces represent 20% and 2.5% of the maximum density. All atoms reside in the left part of the double-well, and the entire density profile is located in the minimum of the left well. Depending on the relative interaction strength ϵ_{dd} the dBEC in the left well features (a), (d) a regular SF for $\epsilon_{dd} = 1.31$, (b) an elongated ($\epsilon_{dd} = 1.4$) or (e) planar SS ($\epsilon_{dd} = 1.49$), (c) an elongated DL pattern for $\epsilon_{dd} = 1.49$ as well as (f) a single droplet surrounded by a homogeneous density distribution for $\epsilon_{dd} = 1.559$. Notice that the individual transitions are shifted to larger ϵ_{dd} from the quasi-1D to the quasi-2D setting. The tilt strength is $D = 7 \hbar \omega_x / l_{\text{osc}}$ enforcing all $N = 40\,000$ magnetic atoms to reside on the left part of the double-well. The left part of the double-well is characterized by frequencies (a)–(c) $(\omega_x, \omega_y, \omega_z) = 2\pi \times (19, 53, 81)$ Hz and (d)–(f) $(\omega_x, \omega_y, \omega_z) = 2\pi \times (43, 43, 131)$ Hz, while having a width $w = 0.5 l_{\text{osc}}$ and height $V_D = 10 \hbar \omega_x$. The potential contours at $z = 0$ plane for $D = 7 \hbar \omega_x / l_{\text{osc}}$, along with the variation of the potentials $V(x, 0, 0)$ across x for $D = 7 \hbar \omega_x / l_{\text{osc}}$ (solid line) and $D = 0$ (dashed line), are shown in the left and right panels for elongated and pancake-like single-wells, respectively.

to (ii) a pancake double-well with circular single wells, $(\omega_x, \omega_y, \omega_z) = 2\pi \times (43, 43, 133)$ Hz (as in Ref. [53]). The lowest panels of Fig. 1 show the contours of the potentials cut through $z = 0$ for $D = 10 \hbar \omega_x / l_{\text{osc}}$. Also, Figs. 1(a)–1(f) represent the dBEC configurations in the left well before the quench for the elongated and planar single wells, respectively. The characteristic timescales determined by the trap frequency accordingly correspond to $\omega_x^{-1} = 8.4$ ms and $\omega_x^{-1} = 3.7$ ms in the elongated and planar cases, with harmonic oscillator lengths $l_{\text{osc}} = \sqrt{\hbar / (m\omega_x)} = 1.8 \mu\text{m}$ and $1.2 \mu\text{m}$, respectively. Another important timescale is set by the energy difference among the pre and postquench states, $\tau_{D_{\text{in}}} = 1 / \Delta \mathcal{E}_{D_{\text{in}}}$, where $\Delta \mathcal{E}_{D_{\text{in}}} \equiv \mathcal{E}_{D_{\text{in}}} - \mathcal{E}_{D_{\text{fi}}}$. Here, $\mathcal{E}_{D_{\text{in}}}$ and $\mathcal{E}_{D_{\text{fi}}}$ refer to the energy of the dBEC at the initial ($D_{\text{in}} = D$) and final ($D_{\text{fi}} = 0$) tilt strengths. The interaction dependence of

$\Delta \mathcal{E}_{D_{\text{in}}}$ is weak for the considered values of ϵ_{dd} . We thus provide an average value for each D_{in} . In this sense, relevant timescales obtained from this energy difference correspond to $\tau_{D_{\text{in}}=10} \approx 40$ ms and $\tau_{D_{\text{in}}=7} \approx 20$ ms in both settings.

In what follows, we explore a ^{164}Dy dBEC under the influence of the energy offset for specific values of ϵ_{dd} corresponding to a SF, a SS, and a DL in the initial state. After preparing the initial configuration, we perform a quench of the tilt strength from a finite value to zero, and monitor the system dynamics as the energy offset vanishes for up to 1 second.

III. INITIAL STATES IN THE TILTED DOUBLE-WELL

Let us begin by investigating the ground-state phases of the dBEC as sketched in Fig. 1. For simplicity, we employ a tilt strength $D = 7 \hbar \omega_x / l_{\text{osc}}$ providing an energy offset among the wells which ensures that the entire dBEC is initially trapped in the left part of the potential. To obtain the ground states, we employ the imaginary time propagation method in the eGPE of Eq. (1) using the split-step Crank-Nicolson [68] approach (see also Appendix C). Characteristic isosurfaces of the three-dimensional density $n(x, y, z)$ are shown in Fig. 1 for different values of ϵ_{dd} . Recall that the integrated spatial density distribution (over tightly confined directions) showcasing crystal arrays can be experimentally probed by *in situ* imaging [27,57].

The structural configurations depend on both the magnitude of ϵ_{dd} and the confinement geometry. For relatively small values of ϵ_{dd} such as $\epsilon_{dd} \approx 1.31$ where the contact interaction dominates over the long-range anisotropic dipolar interaction, a nonmodulated SF state emerges. It is characterized by the typical homogeneous density profile along the x direction [Fig. 1(a)] for the elongated single well, and a pancake distribution in the x - y plane [Fig. 1(d)] in the circular single well, respectively. The distributions are compressed across the tightly confined directions along y and z in the elongated trap and across the z direction in the case of the planar trap, see Sec. II. As expected, in both cases, the SF state has positive energy and chemical potential, here, for $D = 7 \hbar \omega_x / l_{\text{osc}}$ [see also Fig. 2(a)].

Increasing ϵ_{dd} while maintaining the confinement and dipolar direction eventually renders the system self-bound, characterized by a negative chemical potential. For instance, when $\epsilon_{dd} \approx 1.4$ for the elongated single-well (and similarly, for $\epsilon_{dd} = 1.49$ in the case of the pancake-like double-well) we observe the formation of a periodic, density-modulated pattern in the left well.¹ The individual density peaks² are phase-coherently interlinked by a coherent background SF and a SS state forms. For larger ϵ_{dd} , the dipolar interactions

¹Concerning a state of the dBEC that is entirely trapped in one of the wells, the transition from the SF towards the SS and DL phases can also be seen in the momentum distribution where, in contrast to the single-peak structure of the SF, additional higher-lying ones accumulate in both the SS and droplet regimes.

²The number of the generated density humps increases for larger atom number while keeping all other system parameters fixed as it was also discussed, e.g., in Ref. [38]. These structures appear in the transverse direction as elongated filaments.

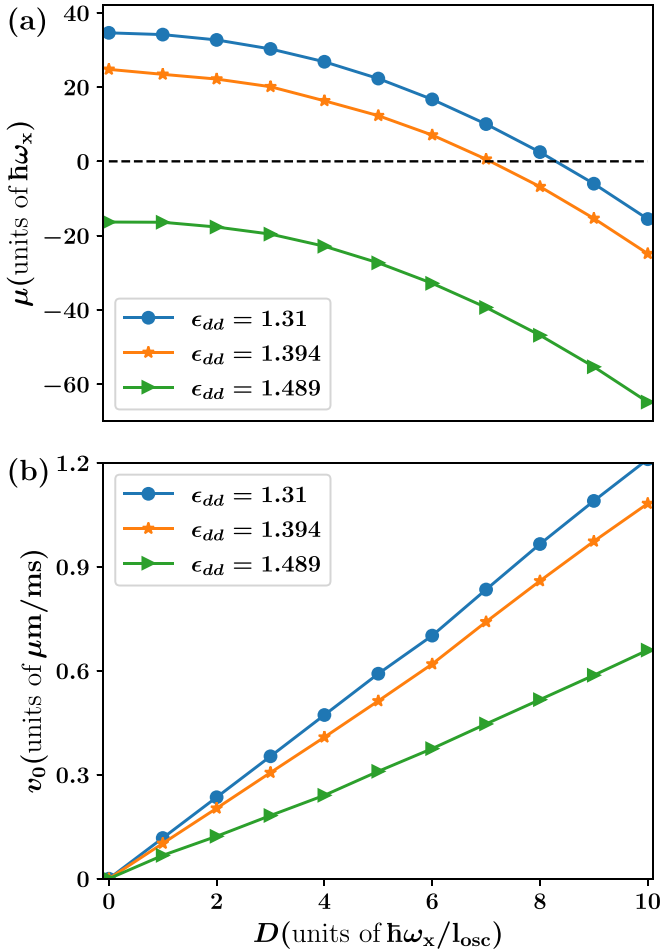


FIG. 2. (a) Dependence of the dBEC chemical potential in the elongated double-well for varying tilt strength D and specific relative interaction coefficients ϵ_{dd} (see legend). The interplay among D and ϵ_{dd} dictates the ground-state phases from SF to SS and droplet lattice. (b) The initial velocity $v(0) \equiv v_0$ of the dBEC center of mass as a function of the tilt strength for several ϵ_{dd} (see legend). It features an interaction-dependent linear behavior with the SF ($\epsilon_{dd} = 1.31$) possessing a larger velocity. The modification in the slope of v_0 around $D = 6 \hbar\omega_x/l_{\text{osc}}$ occurs since, above this value, the entire dBEC is located at the left part of the double-well.

become dominant. This leads to a vanishing SF background and a simultaneous stronger spatial localization of the aforementioned density humps, see Figs. 1(c) and 1(f). In this droplet phase, the self-bound character is related with large negative energy or equivalently chemical potential [Fig. 2(a)]. Figure 1(c) depicts a characteristic DL density distribution in an elongated geometry. However, in the planar geometry, instead, a central droplet is surrounded by a ring-shaped SF configuration, see Fig. 1(f), as discussed in Ref. [23].

Increasing the energy offset favors the DL formation and can lead to a negative chemical potential [Fig. 2(a)]. The offset thus also enables a crossover to self-bound states in the double-well. For a smaller energy offset between the wells a certain fraction of population can still reside in the right part of the double-well. The interaction-dependent critical tilt value, where the entire cloud is solely trapped in the left well, is lower for larger ϵ_{dd} , e.g., $D < 4 \hbar\omega_x/l_{\text{osc}}$ for $\epsilon_{dd} =$

1.49, and increases for reduced ϵ_{dd} , e.g., $D < 6 \hbar\omega_x/l_{\text{osc}}$ for $\epsilon_{dd} = 1.36$. Furthermore, through the adjustment of D , it is possible to prepare more intricate density patterns arising from populations located in both wells. For instance, when $D = 2 \hbar\omega_x/l_{\text{osc}}$, two droplets form in the left well, while a single-slanted DL structure appears in the right well. Such configurations, influenced by interference and restricted initial velocities dictated by the value of D , have a significant impact on the resulting dynamical behavior, as will be discussed in the following.

IV. DYNAMICS IN AN ELONGATED DOUBLE-WELL

To explore the dynamical properties of the dBEC in a double-well, we first consider an elongated geometry along the x direction. The system is quenched by instantaneously (at $t = 0$) switching off the external tilt, from a value $D > 0$ to $D = 0$. For the impact of a time-dependent ramp-down of the tilt on the tunneling dynamics and the persistence of the discussed tunneling regimes for different ramp rates, see Appendix B. Naturally, the strength of the tilt potential is related to the initial velocity imparted on the dBEC directly after performing the $D = 0$ quench. Namely, a larger initial D refers to an increasing velocity. This can be readily verified by determining the velocity of the center of mass of the dBEC, $v(t = 0) \equiv v_0$, provided in Fig. 2(b) for various interactions as a function of D . The velocity herein is defined as the time derivative of the center-of-mass coordinate $X_{\text{CM}}(t) = \int_{-x_0}^{x_0} dx x n_{1\text{D}}(x, t)$, where $n_{1\text{D}}(x, t) = \int dy dz n(x, y, z, t)$ denotes the one-dimensional (1D) integrated density and $\pm x_0/2$ is the location of the employed hard-wall boundaries along the x direction. These are, of course, chosen sufficiently wide such that they do not affect our results. The dependence of v_0 on the interaction strength is clearly seen. For larger ϵ_{dd} values and a fixed D , i.e., towards the droplet regime, the velocity decreases, reflecting the rigidity of the state.

To visualize the overall dynamical response of the elongated dBEC we invoke the underlying integrated density, $n_{1\text{D}}(x, t)$ (Fig. 3). Moreover, to determine the emergent tunneling behavior, we monitor the population imbalance [65] among the left (L) and right (R) wells

$$\begin{aligned} \Delta\mathcal{N}(t) &= \frac{1}{N} \left[\int_{-x_0/2}^0 dx n_{1\text{D}}(x, t) - \int_0^{x_0/2} dx n_{1\text{D}}(x, t) \right] \\ &\equiv n_L(t) - n_R(t). \end{aligned} \quad (3)$$

It allows to estimate both the frequency and amplitude of the induced macroscopic tunneling properties.

As a starting point, we leverage a relatively large tilt strength, $D \geq 10 \hbar\omega_x/l_{\text{osc}}$, rendering the impact of the initial velocity v_0 [which is enhanced here, Fig. 2(b)] irrelevant. Indeed, for $D \geq 10 \hbar\omega_x/l_{\text{osc}}$, the entire dipolar gas is localized in the left double-well rendering the quench-induced tunneling process independent of the tilt strength. This enables us to unravel the ensuing interaction effects on the dynamics. Ramping-down D leads to coherent oscillations of the dBEC with a frequency that is weakly dependent on the relative interactions ϵ_{dd} , see Figs. 3(a1)–3(a3) and Fig. 4(b). Notice, however, that the oscillation amplitude is reduced for increasing ϵ_{dd} , see also the discussion below and Fig. 4(b). In the

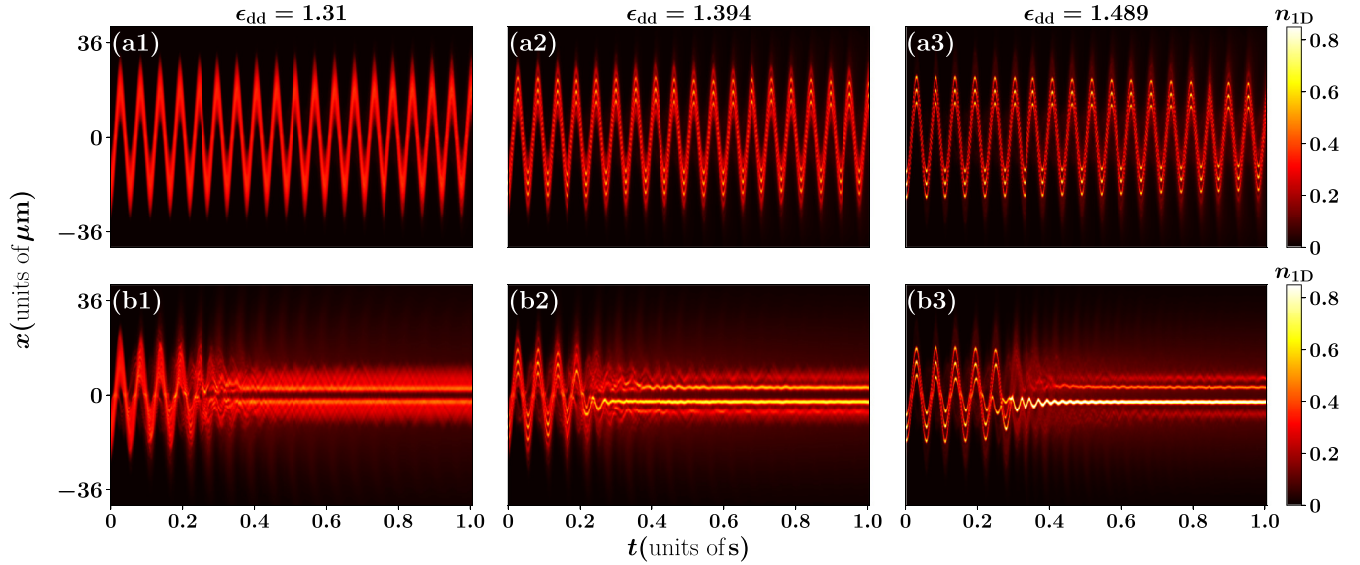


FIG. 3. Dynamics in the elongated double-well, triggered by quenching the tilt strength from (a1)–(a3) $D = 10 \hbar\omega_x/l_{\text{osc}}$ and (b1)–(b3) $D = 7 \hbar\omega_x/l_{\text{osc}}$ to $D = 0$. In the panels from left to right, the system is in the SF with $\epsilon_{\text{dd}} = 1.31$, a SS characterized by $\epsilon_{\text{dd}} = 1.394$ and a droplet array with $\epsilon_{\text{dd}} = 1.489$, respectively. The colorbar represents the integrated density $n_{1\text{D}}(x, t)$ after the quench in units of N/l_{osc} , where $N = 40\,000$ and $l_{\text{osc}} = 1.80 \mu\text{m}$. The tunneling frequency is nearly unaltered for different values of ϵ_{dd} , but the amplitude is reduced for increasing ϵ_{dd} . It is evident that the tunneling properties of the dBEC depend strongly on its initial velocity as quantified by the initial D value, i.e., for decreasing D the dBEC density smudges over both wells for longer evolution times.

case of a SF ($\epsilon_{\text{dd}} \approx 1.31$) the entire dBEC coherently moves between the left and right wells with constant amplitude and period³ $T_{\text{Rabi}} \approx 55$, in analogy to what is known for regular BECs [62,63]. This response will be dubbed the macroscopic collective tunneling regime.

A similar dynamical behavior is also observed for a SS [Fig. 3(a2) for $\epsilon_{\text{dd}} = 1.397$] and a droplet array [Fig. 3(a3) for $\epsilon_{\text{dd}} = 1.49$]. Initially being localized in the left well, after quenching, the SS or DL crystal structures move towards the right side, and during this process come into close proximity with each other, particularly in the vicinity of the potential barrier [see Figs. 3(a2) and 3(a3)]. Subsequently, the crystals move into the right well, and as they reach the right well's edge they separate from each other again. This process repeats periodically. The maximum separation between the single crystals at the well's edge is more pronounced for larger ϵ_{dd} due to the dominant dipolar interactions, which enhance repulsion among the density humps in the transverse plane [see Figs. 3(a3) and 3(b3)].

A reduction of the tilt strength [or equivalently the initial velocity, Fig. 2(b)] leads to significant alterations of the dynamical behavior. Comparing Figs. 3(a1)–3(a3) with Figs. 3(b1)–3(b3) reveals a different response, displaying intricate tunneling dynamics. At short evolution times, $t \approx \tau_{D_{\text{in}}=7}$, the dBEC oscillates back and forth between the wells. However, owing to the reduced velocity at $t = 0$, the dBEC

gradually starts to be partially transmitted to the other well while a relatively small fraction is reflected back. As more particles are reflected in the course of the evolution, individual density humps become less prominent both in the SS [Fig. 3(b2)] and the DL [Fig. 3(b3)]. Eventually, after four oscillation periods ($t \gg \tau_{D_{\text{in}}=7}$) a certain population remains trapped within each well and tunneling locks. Indeed, employing $D = 7 \hbar\omega_x/l_{\text{osc}}$ which still ensures the confinement of the dBEC within the left well at $t = 0$, we observe that the smaller initial velocity (as compared to the case with $D = 10 \hbar\omega_x/l_{\text{osc}}$) results in a gradual suppression of the interwell tunneling, see also $\Delta\mathcal{N}(t)$ in Fig. 4(a). A further decrease of D favors an appreciable part of the population to initially also reside in the right well. This eventually leads to suppression of the tunneling due to the relatively weak exerted momentum by the quench, see the values of $\Delta\mathcal{N}(t)$ for $D = 2 \hbar\omega_x/l_{\text{osc}}$, for example, in Fig. 4(a). This resembles a type of self-trapping, as it has been also realized in regular BECs [59,62,69,70].

For larger ϵ_{dd} , different droplet lattice configurations can be realized in the left well compared to the right well. In this case, the individual crystals or SSs undergo multifrequency intrawell oscillations of varying amplitude induced by the tunneling of the background SF, see also the explicit time evolution in Ref. [71]. We note here that removing the small offset between the wells is essentially equivalent to imparting a small kick velocity to the crystal structures. The vibrational patterns emanate from the activation of the different underlying normal modes, as demonstrated in Ref. [72]. The main features of the above-described tunneling behavior remain robust (at least up to certain times) even in the presence of three-body losses, which are customarily present in experiments, as showcased in Appendix A. However, in this case the tunneling is suppressed for longer evolution times and, e.g., the SS or DL character is lost due to atom losses.

³Notice that $T_{\text{Rabi}} \sim 2\pi/(\omega_x)$ for large D , meaning that the tunneling is essentially a collective center-of-mass oscillation, i.e., the dipole mode. However, a more accurate estimation of the tunneling period for all D examined herein would require knowledge of the ensuing energy gap among the wells. In this context, a larger gap enforced by increasing tilt strength leads to a smaller period.

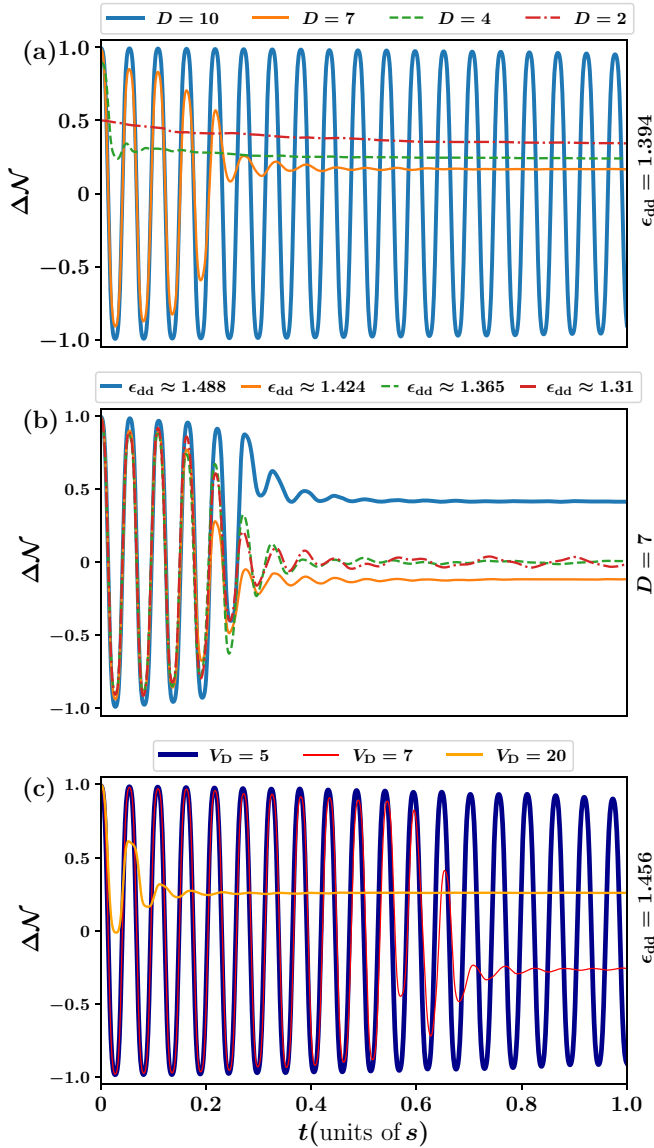


FIG. 4. Time evolution of the population imbalance $\Delta\mathcal{N}(t)$ between the left and right wells for (a) different initial tilts D (see legend) at fixed $\epsilon_{dd} = 1.394$ referring to a SS and (b) distinct relative interactions, ϵ_{dd} (see legend) when $D = 7\hbar\omega_x/l_{osc}$. It is evident that a decreasing tilt strength slows down tunneling, while for a constant D population imbalance at long evolution times is suppressed only within the SF phase and becomes maximal for a droplet array. (c) $\Delta\mathcal{N}(t)$ in the SS case with $\epsilon_{dd} = 1.456$ and using an initial $D = 7\hbar\omega_x/l_{osc}$ for several barrier heights V_D (see legend). An increasing V_D leads to a macroscopic self-trapping regime. The dBEC consists of $N = 40\,000$ ^{164}Dy atoms confined in a quasi-1D double-well. The tilt strength D of the double-well is measured in units of $\hbar\omega_x/l_{osc}$.

A smudging of density occurs for the SF, SS, and DL regimes as can be readily seen by inspecting the population imbalance, $\Delta\mathcal{N}(t)$, shown in Fig. 4(b) for varying ϵ_{dd} and fixed $D = 7\hbar\omega_x/l_{osc}$. In particular, we deduce that the condensate density smudges at a faster rate for a SS ($\epsilon_{dd} = 1.424$) as compared to the other phases, an outcome that is attributed to the enhanced interference of the individual crystals due to

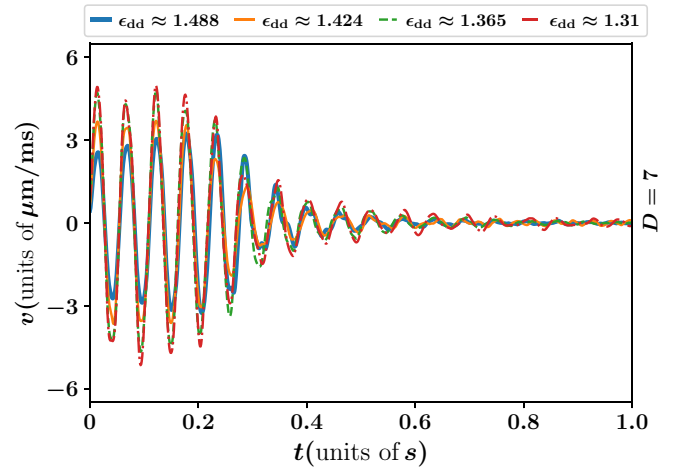


FIG. 5. Dynamics of the velocity, $v(t)$, of the dBEC center-of-mass coordinate for various ϵ_{dd} (see legend) keeping $D = 7\hbar\omega_x/l_{osc}$. Apparently, upon considering fixed D and increasing ϵ_{dd} towards the droplet regime leads to a progressively smaller velocity signifying the crystalline nature of the dBEC. At long evolution times the dBEC relaxes and its velocity vanishes. The tilt strength D of the double-well is expressed in terms of $\hbar\omega_x/l_{osc}$.

the background SF.⁴ Moreover, the population imbalance in the long time evolution after the termination of the tunneling is found to depend on the dBEC phase and thus the interactions. With increasing ϵ_{dd} , atoms exhibit a stronger tendency to self-bind, leading to their preferential accumulation within a specific well in the long time evolution and causing a more pronounced atom imbalance. A larger dilute SF component, occurring for weaker ϵ_{dd} , however, facilitates the progressive restoration of interwell population balance. As such, $\Delta\mathcal{N}(t)$ in the course of the tunneling may serve as a probe to identify the crystalline nature of the dBEC. The suppression of the tunneling is also supported by the behavior of the velocity of the center of mass showcased in Fig. 5. Keeping the initial tilt strength fixed, for example, at $D = 7\hbar\omega_x/l_{osc}$, the velocity in the course of the dBEC evolution is overall reduced towards the self-bound state regime realized for larger ϵ_{dd} . This can be traced back to the enhanced rigidity of the droplet arrays.

Naturally, the barrier height has a crucial impact on the tunneling, as is also known from short-range interacting BECs [59,60,65]. To explicate this dependence we consider a SS state at $\epsilon_{dd} = 1.456$ experiencing a tilt of $D = 7\hbar\omega_x/l_{osc}$ and measure $\Delta\mathcal{N}(t)$ for various V_D presented in Fig. 4(c). It becomes apparent that by increasing V_D , which equivalently means that the involved energy gaps become larger [59], it is possible to transition to distinct tunneling regions. In other words, it is possible to adjust the dBEC response from coherent density oscillations, as here for $V_D = 5\hbar\omega_x$, to density smudging and tunneling locking at long times, for instance,

⁴The same observations in terms of the tunneling regimes can be made by inspecting the dynamics of the integrated current $J(t) = \frac{\hbar}{2mi} \int dx dy dz (\Psi^* \frac{\partial \Psi}{\partial x} - \Psi \frac{\partial \Psi^*}{\partial x})$, not shown for brevity.

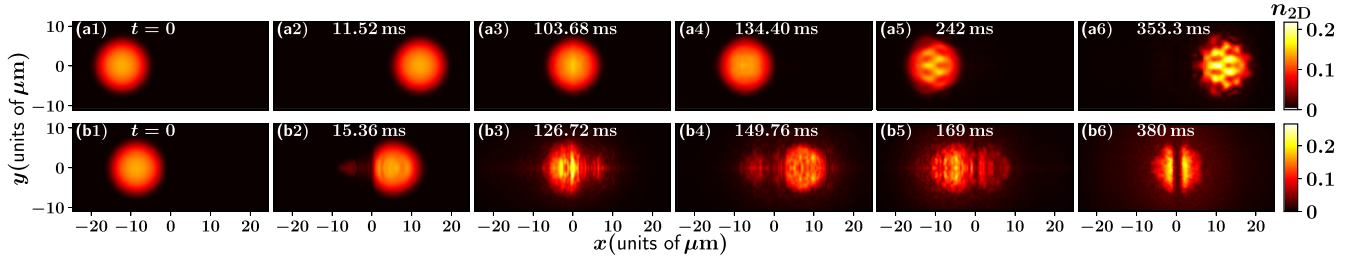


FIG. 6. Snapshots of the integrated 2D density $n_{2D}(x, y, t)$ visualizing the tunneling of a SF configuration for $\epsilon_{dd} = 1.31$ when the initial strength of the double-well is set to (a1)–(a6) $D = 10 \hbar\omega_x/l_{osc}$ and (b1)–(b6) $D = 7 \hbar\omega_x/l_{osc}$. The tunneling behavior depends on the original D value. For $D = 10 \hbar\omega_x/l_{osc}$, i.e., large initial velocities, it leads to persistent oscillations of the SF among the wells and its motional excitation at longer evolution times. However, a reduced velocity (here quantified by $D = 7 \hbar\omega_x/l_{osc}$) results in a progressive damping of the tunneling and its subsequent locking. The evolution is induced by suddenly suppressing the tilt strength. The colorbar signifies $n_{2D}(x, y, t)$ in units of N/l_{osc}^2 , where $N = 40\,000$ and $l_{osc} = 1.2 \mu\text{m}$.

when $V_D = 7 \hbar\omega_x$, and vanishing interwell tunneling at $V > 20 \hbar\omega_x$.

V. DYNAMICS IN A PANCAKE DOUBLE-WELL

Let us now investigate how the above-described phenomena depend on the dimensionality of the system and turn to the pancake-like double-well. The dBEC is initialized in the tilted double-well assembling in different configurations according to the value of ϵ_{dd} as depicted in Figs. 1(d)–1(f). As before, the time evolution is induced via quenching the tilt strength D from a finite value down to $D = 0$. Similar to the elongated geometry [Fig. 2(b)], the initial velocity, v_0 , exhibits a linear increase for larger D and fixed ϵ_{dd} , while being reduced for larger ϵ_{dd} and constant D (not shown). The overall dynamical behavior is characterized through the two-dimensional (2D) integrated density defined as $n_{2D}(x, y, t) = \int dz n(x, y, z, t)$ and the respective population imbalance $\Delta \mathcal{N}(t) = (1/N) [\int_{-x_0/2}^0 \int_{-y_0}^{y_0} dx dy n_{2D}(x, y, t) - \int_0^{x_0/2} \int_{-y_0}^{y_0} dx dy n_{2D}(x, y, t)]$, with $\pm x_0/2$ [$\pm y_0/2$] denoting the position of the hard walls in the x (y) direction.

Considering a large energy offset at $t = 0$, quantified by $D = 10 \hbar\omega_x/l_{osc}$, we find that irrespective of ϵ_{dd} the entire dBEC undergoes regular oscillations between the left and right wells with constant amplitude and frequency throughout the time evolution. This behavior can be directly seen in the densities of a SF (SS) depicted in Figs. 6(a1)–6(a6) [Figs. 7(a1)–7(a6)], but also in the corresponding interwell

population imbalance provided in Fig. 8(a) exemplary for the SF case. Focusing on the evolution of the SF state with $\epsilon_{dd} = 1.31$, there are two main distinct dynamical stages: At early evolution times, the SF coherently oscillates back and forth characterized by a Rabi frequency $T_{\text{Rabi}} \approx 24 \text{ ms} \approx 2\pi/\omega_x$ and without experiencing any noticeable density deformation. While later on [Figs. 6(a5) and 6(a6)], the density distortion gradually enhances, likely due to the trigger of underlying collective modes [35–37,73] after multiple collisions of the condensate with the central barrier.

The tunneling behavior of a SS configuration obtained at $\epsilon_{dd} \approx 1.49$ with fixed $D = 10 \hbar\omega_x/l_{osc}$ is demonstrated in Figs. 7(a1)–7(a6). Interestingly, we observe the persistent interwell oscillatory motion as well as the angular oscillation of the entire SS. However, the original SS retains its shape throughout the time evolution with the background superfluid exhibiting spatial undulations [Figs. 7(a3) and 7(a4)] stemming, in part, from the particle flow between the constituting crystals and, in part, from the collision with the central barrier. The above response substantiates the rigidity of the droplet crystal arrangement, with the distance of the crystals remaining almost intact, and the dilute superfluid nature of the background. Indeed, the involved droplet crystals share a relatively small density overlap leading to debilitated particle flow among the droplets. As a consequence, the atom number within each droplet is not appreciably modified in the time evolution.

As in the elongated geometry, a reduction of the initial tilt strength leads to significant modifications of the tunneling

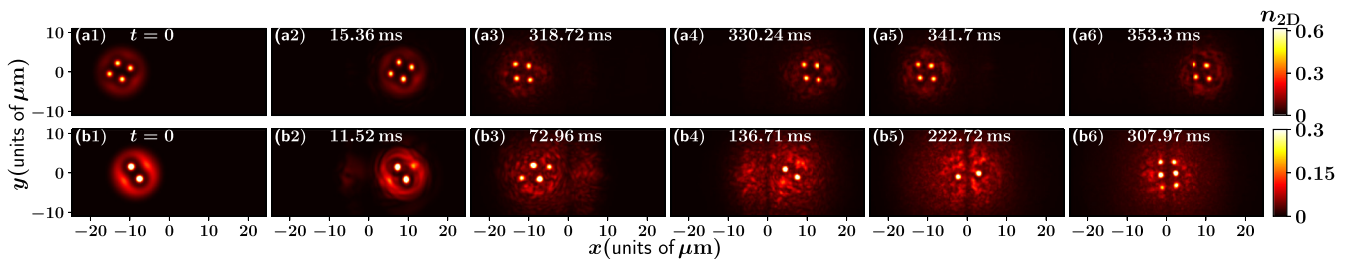


FIG. 7. Density snapshots demonstrating the tunneling behavior of a SS for $\epsilon_{dd} \approx 1.49$ using an initial interwell energy offset characterized by (a1)–(a6) $D = 10 \hbar\omega_x/l_{osc}$ and (b1)–(b6) $D = 7 \hbar\omega_x/l_{osc}$. In the case of $D = 10 \hbar\omega_x/l_{osc}$, the SS oscillates back and forth maintaining its shape with the involved crystals featuring quadrupole excitations. In contrast, for $D = 7 \hbar\omega_x/l_{osc}$ dynamically unstable crystals appear in the course of the evolution and eventually at long-time tunneling locks. The colorbar represents $n_{2D}(x, y, t)$ in terms of N/l_{osc}^2 , with $N = 40\,000$ and $l_{osc} = 1.2 \mu\text{m}$.

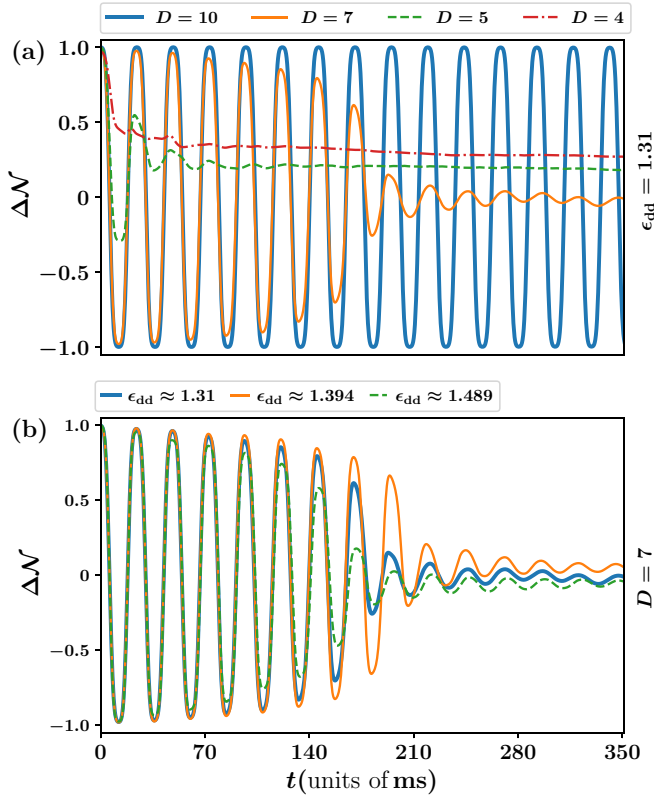


FIG. 8. Dynamics of the interwell population imbalance $\Delta\mathcal{N}(t)$ in the quasi-2D double-well when considering (a) various tilt strengths D (see legend) and $\epsilon_{dd} = 1.31$ corresponding to a SF or (b) using different ϵ_{dd} (see legend) and $D = 7\hbar\omega_x/l_{osc}$. A reduced energy offset results to a gradual suppression of tunneling. Moreover, $\Delta\mathcal{N}(t)$ in the region of D where tunneling locks vanishes within the SF phase but it remains finite in the SS. The evolution of the quasi-2D dBEC with $N = 40\,000$ ^{164}Dy atoms is triggered by quenching the initial potential offset D to zero.

behavior due to the comparatively smaller initial velocity. Characteristic instantaneous density profiles of a SF dBEC ($\epsilon_{dd} = 1.31$) following a quench from $D = 7\hbar\omega_x/l_{osc}$ to $D = 0$ are provided in Figs. 6(b1)–6(b6). It can be readily seen that the SF tunnels from the left to the right well [Figs. 6(b1) and 6(b2)], but the initial velocity is not sufficient for the entire cloud to be fully transmitted. As such, there is a fraction of reflected density remaining back and becoming more pronounced during the dynamics; see, for example, Figs. 6(b3)–6(b5), which are characterized by enhanced spatial delocalization. This progressive collocation of density in both wells results in a vanishing population imbalance and tunneling “locks” as visualized in the density snapshot of Fig. 6(b6) and explicitly captured via $\Delta\mathcal{N}(t)$ in Fig. 8(a). We remark that using smaller initial energy offsets, viz., $D \leq 5\hbar\omega_x/l_{osc}$ the distribution of the dipoles takes place in both the left and right wells. Following a quench to $D = 0$ leads to suppression of tunneling as can be deduced from $\Delta\mathcal{N}(t)$, illustrated in Fig. 8(a) for $D = 5\hbar\omega_x/l_{osc}$ and $D = 4\hbar\omega_x/l_{osc}$, and eventually to solely intrawell dynamics of the underlying density fractions; see also Ref. [74].

Similar effects occur even when a SS is considered with smaller tilt. In Figs. 7(b1)–7(b6), we demonstrate 2D densities

at different time-instants for $\epsilon_{dd} = 1.49$. For $D = 7\hbar\omega_x/l_{osc}$, the initial SS possesses only two humps [Fig. 7(b1)]. When performing the $D = 0$ quench, the crystals, at early evolution times, oscillate together back and forth between the two wells, keeping their distance almost fixed. Simultaneously, a fraction of atoms is reflected from the barrier. Such reflection and transmission phenomena give rise to unequal populations in both wells during the dynamics. As a consequence, there are various unstable droplet configurations, such as the rhombic one depicted in Fig. 7(b3), or two droplet configurations [Figs. 7(b4) and 7(b5)], appearing during the dynamics. In the long time ($t > 310$ ms) dynamics, atoms gradually accumulate in both wells in a symmetric manner and a three-droplet configuration in each well can be seen on either side [Fig. 7(b6)]. Consecutively, tunneling locks with a small interwell population imbalance as shown in Fig. 8(b). It is important to mention that the robustness of the SS structure during the tunneling dynamics depends strongly on the presence of the background SF which connects the individual crystals. Indeed, a more pronounced SF background eases particle transfer between the crystals, thus rendering them more susceptible to distortions and making them less rigid.

VI. CONCLUSION AND PERSPECTIVES

We investigated the ground state and the tunneling dynamics of a dBEC trapped in an initially tilted double-well potential encompassing both elongated and pancake trap geometries. To model these systems and their dynamical behavior, we employed the extended Gross-Pitaevskii framework that incorporates first-order quantum corrections. The different phases are initialized by tuning the relative strength ratio between dipolar and short-range interactions while maintaining the tilt strength. The interwell energy offset imposed by the tilt strength effectively modifies the trapping volume of the dBEC. Thus, even for fixed interactions, when changing the tilt strengths a transition from a SF to SS and DL state may occur, decreasing the chemical potential to negative values. The tilt value, furthermore, governs the initial center-of-mass velocity of the dBEC. For larger offsets and fixed interactions, the velocity monotonically increases. Conversely, for a specific tilt and varying interactions, the velocity decreases as the system transitions from the SF phase towards the SS and DL phases, evincing the rigidity of the latter.

The time-evolution of the system is initiated by suddenly releasing the initial interwell energy offset, promoting the tunneling motion of the dBEC. For the elongated double-well, it is observed that for sufficiently large tilt strengths, the dBEC, regardless of being in the SF, SS, or DL phase, undergoes collective oscillations with a definite amplitude and frequency. However, a smaller initial energy offset leads to the partial transmission and reflection of the dipoles during the dynamics. The resultant interference of these accumulated density fractions gives rise to a smudging of the density, evident in the intrawell population, and eventually tunneling locks. In this dynamical stage, the interwell population imbalance is highly asymmetric for the droplet array, while it vanishes in the SF case. This characteristic provides a valuable means to investigate the nature of the individual phases. The rigidity of the crystal-like SS and droplet configurations is further

supported by their smaller center-of-mass velocity compared to the SF phase during the dynamics. Maintaining fixed interactions and tilt strength but increasing the barrier height, the dipoles consequently remain confined within the initial well.

A similar dynamical response in terms of the aforementioned system parameters also takes place in quasi-2D, but there are characteristic properties that are inherently related to the dimensionality of SS and DL. Indeed, for sufficiently large tilt strengths the dBEC undergoes regular oscillations back and forth among the wells. It also features distinctive dynamical patterns depending on the interactions. A SS with suppressed background SF tunnels as a whole, maintaining its initial configurations which substantiates its rigidity. This motion is accompanied by small-amplitude angular oscillations triggered by the quench. Exploiting a reduced energy offset leads to partial transmission events of the dipolar cloud and ultimately to tunnel locking caused by collocation of density in each well during the evolution. This dynamical regime is characterized by vanishing interwell population imbalance.

There is a variety of possible extensions of our results in future endeavors. An imperative prospect is to testify the validity of the eGPE to adequately describe all the emergent tunneling channels. Along these lines, it is worth unraveling the participation of possible interband tunneling processes, especially in the few- to many-body crossover relying, for instance, in *ab initio* methods [75,76]. In this context, it would be possible to achieve an accurate characterization of the induced tunneling pathways in terms of the relevant energy gaps and possibly reveal higher-order, e.g., interband, tunneling channels. Additionally, the inclusion of temperature and its impact on the discussed tunneling properties is worth pursuing. A first step towards this direction could be to utilize a stochastic Gross-Pitaevskii model as was done in Ref. [39]. Exploiting dynamical frustration events, e.g., by ramping a lattice potential in SS and DL [43], to design exotic tunneling processes is another intriguing direction. The spontaneous generation of nonlinear wave structures stemming from the counterflow dynamics of two initially separated dBEC clouds is certainly desirable. Furthermore, a detailed study of the excitation of corresponding surface modes in dBECs (for example, using parametric driving as it was achieved in regular BECs [77,78]) constitutes another interesting future prospect.

ACKNOWLEDGMENTS

S.I.M. and H.R.S. acknowledge support from the NSF through a grant for ITAMP at Harvard University. K.M. and S.M.R. are financially supported by the Knut and Alice Wallenberg Foundation (KAW 2018.0217) and the Swedish Research Council (2022-03654_VR).

APPENDIX A: IMPACT OF THREE-BODY RECOMBINATION IN THE TUNNELING DYNAMICS

The self-bound SS and droplet configurations are known to feature appreciable three-body losses [34,79] whose presence naturally destructs, in the experiment, the long-time observation and characteristics of these structures. For this reason, in what follows, we aim to expose the effect of the three-body loss rate in the tunneling properties, e.g., of the elongated SS at $\epsilon_{\text{dd}} = 1.394$. To monitor the ensuing dynamics we

rely on the eGPE of Eq. (1) using the additional imaginary term $-(i\hbar K_3/2)|\psi(\mathbf{r}, t)|^4\psi(\mathbf{r}, t)$, where K_3 refers to the three-body recombination rate [50,80,81]. As a reference point of the recombination rate coefficient we consider $K_3 = 1.2 \times 10^{-40} \text{ m}^6/\text{s}$ which was identified in the experiment in Ref. [9]. For a discussion about the interplay of three-body recombination and beyond mean-field contributions see the review of Ref. [7].

The density evolution visualizing the emergent tunneling dynamics of the initially prepared SS in a tilted double-well for different energy offsets $D = 10 \hbar\omega_x/l_{\text{osc}}$ and $D = 7 \hbar\omega_x/l_{\text{osc}}$ is illustrated in Figs. 9(a) and 9(b), respectively. As it can be deduced, the presence of three-body losses does not prevent the observation of the tunneling processes taking place at early timescales $t < 200 \text{ ms}$ that were discussed in the main text, see also Figs. 3(a2) and 3(b2). Namely, for $D = 10 \hbar\omega_x/l_{\text{osc}}$ oscillations of the SS between the wells occur. Also, in the case of $D = 7 \hbar\omega_x/l_{\text{osc}}$ despite the overall collective tunneling behavior there are certain reflected portions of the SS simultaneously with each transmission event. In the course of the evolution they accumulate, and their interference leads to density smudging and locking of the tunneling process.

However, as expected, the underlying atom losses depicted in Fig. 9(c) become more pronounced for longer times ($t \gg \omega_x^{-1}$) resulting ultimately in the destruction of the SS because three-body losses compete with the LHY contribution. This can be readily seen in $n_{1D}(x, t)$ where the individual density humps gradually smoothen and disappear. The dBEC is not able to host a SS at these timescales due to the significant reduction of the atom number, $N(t)$. This decrease of the atom number is, of course, enhanced for larger K_3 coefficients as can also be inferred from Fig. 9(c). However, it also depends on the initial energy offset, see Fig. 9(d), but apparently, there is a nonmonotonic trend with respect to D . This behavior is caused by the peculiar dependence of the peak density on D , which is here the crucial component for the loss rate for fixed K_3 . For instance, at $D = 2 \hbar\omega_x/l_{\text{osc}}$ where the individual crystals are self-trapped in each well, the density is more localized when compared to larger D values as shown in the inset of Fig. 9(d). Therefore, the reduction of $N(t)$ is more rapid in this case. The same argument holds for the other D values. A similar phenomenology occurs also for increasing ϵ_{dd} (not shown), where droplet arrays form. In this case the atom losses are more pronounced due to the relatively higher localized densities related to negative chemical potentials, see also Fig. 2(a).

APPENDIX B: LINEAR RAMPING OF THE ENERGY OFFSET

Another interesting question is whether the above-described tunneling regimes persist in the case of reducing the energy offset in a time-dependent manner or are unique to the quench protocol used. In the following, we argue that indeed the aforementioned tunneling regions can be realized utilizing time-dependent ramps with the latter being sufficiently fast, while closer to the diabatic regime the tunneling is naturally delayed. This investigation allows also to testify the validity of the eGPE predictions after quenching the tilt strength, a

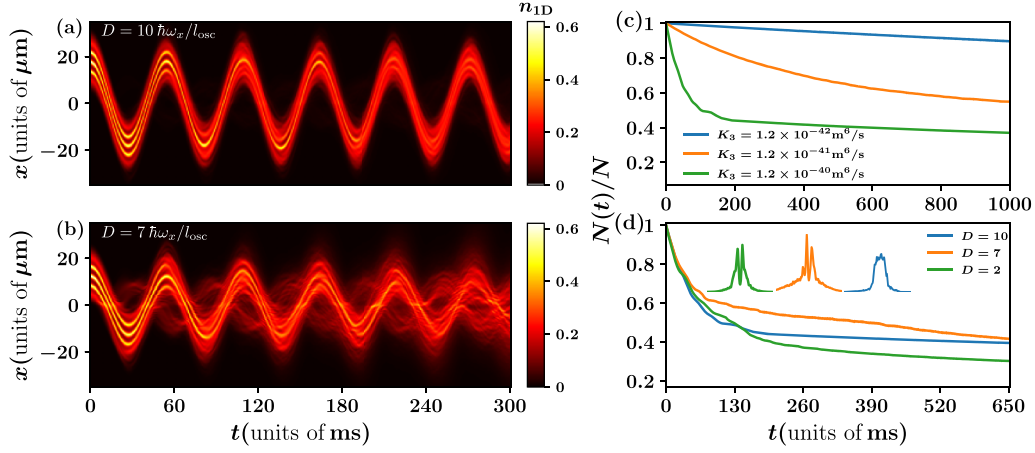


FIG. 9. Time evolution of the integrated density, $n_{1D}(x, t)$, showcasing the tunneling dynamics in the presence of three-body losses with recombination rate coefficient $K_3 = 1.2 \times 10^{-40} \text{ m}^6/\text{s}$ for initial tilt strengths (a) $D = 10 \hbar\omega_x/l_{\text{osc}}$ and (b) $D = 7 \hbar\omega_x/l_{\text{osc}}$. The tunneling processes of the $K_3 = 0$ case persist for early times and afterwards the SS character disappears due to prominent atom losses. The colorbar represents the integrated density $n_{1D}(x, t)$ in units of N/l_{osc} , where $N = 40000$ and $l_{\text{osc}} = 1.80 \mu\text{m}$. Dynamics of the normalized atom number $N(t)/N(t=0)$ for (c) different recombination rate coefficients K_3 (see legend), focusing on $D = 10 \hbar\omega_x/l_{\text{osc}}$ and (d) varying tilt strength D (see legend). As expected, a more prominent reduction of $N(t)$ takes place for larger K_3 . Inset of (d) depicts density profiles, $n_{1D}(x, t)$, at $t = 500 \text{ ms}$ and distinct D values evincing the nontrivial effect of the tilt strength on the density localization. Apparently, the atom loss is crucially affected from the density localization, viz., it is enhanced for larger peak densities. In all cases, the relative interaction parameter $\epsilon_{\text{dd}} = 1.394$.

process that might induce excitations beyond the validity of this approach.

For these reasons, instead of performing a quench of the energy offset, we employ the linear ramp

$$D(t; \tau) = D_{\text{in}} + \frac{(D_{\text{fi}} - D_{\text{in}})t}{\tau}, \quad \text{for } t \leq \tau, \quad (\text{B1})$$

$$D(t; \tau) = D_{\text{fi}}, \quad \text{for } t > \tau. \quad (\text{B2})$$

Here, D_{in} [D_{fi}] denotes the initial (final) tilt strength and τ quantifies the underlying ramp rate. The latter is $\tau \rightarrow 0$ for a quench and $\tau \rightarrow \infty$ for a diabatic change of the energy offset. As in the main text we consider $D_{\text{fi}} = 0$ and for simplicity we restrict our presentation to the quasi-1D setting with $D_{\text{in}} = 7 \hbar\omega_x/l_{\text{osc}}$ and $\epsilon_{\text{dd}} = 1.394$ referring to a SS. To monitor the interwell tunneling features we rely on the population imbalance, $\Delta\mathcal{N}(t)$ in the course of the evolution showcased in Fig. 10. Apparently, we observe that for sufficiently small ramp-rates $\tau < 10 \text{ ms} < \tau_{D_{\text{in}}=7}$, the tunneling behavior is almost identical to the quench scenario, while a larger τ leads to a significantly slower evolution and eventually to suppression of tunneling, i.e., the magnetic atoms tend to remain in the initial well.

APPENDIX C: NUMERICAL SCHEME

To numerically solve the 3D eGPE [Eq. (1)] we make use of the split-time Crank-Nicholson discretization scheme [68,82] and deploy a suitable rescaling. In particular, we transform the 3D wave function as $\Psi(\mathbf{r}', t') = \sqrt{l_{\text{osc}}^3/N} \psi(\mathbf{r}, t)$ and express the time and length in units of the trap frequency ω_x and the harmonic oscillator length $l_{\text{osc}} = \sqrt{\hbar/m\omega_x}$, respectively. The ground state of the dipolar gas is found via the imaginary time propagation method. Due to the many energetically close-lying configurations we employ various

initial guesses to identify the many-body state with the lowest energy. Specifically, in the 1D case the following two different initial guesses $\psi_{1D}(x, y, z) = \mathcal{A}e^{-(x^2+k^2y^2+\lambda^2z^2)/2} \cos^2(l_1x)$ and $\psi_{1D}(x, y, z) = \mathcal{A}e^{-(x^2+k^2y^2+\lambda^2z^2)/2} \sin^2(l_1x)$ are used. The parameters $k^2 = \omega_y/\omega_x$ and $\lambda^2 = \omega_z/\omega_x$ stem from the above-mentioned rescaling. However, for the 2D scenario we invoke the initial guesses $\psi_{2D}(x, y, z) = \mathcal{A}e^{-(x^2+k^2y^2+\lambda^2z^2)/2} (\cos^2(l_1x) + \cos^2(l_2y + \phi))$ and $\psi_{2D}(x, y, z) = \mathcal{A}e^{-(x^2+k^2y^2+\lambda^2z^2)/2} [\sin^2(l_1x) + \cos^2(l_2y + \phi)]$. Here, \mathcal{A} denotes the normalization constant while l_1 , l_2 , and ϕ are varied to realize a different number of crystals in the

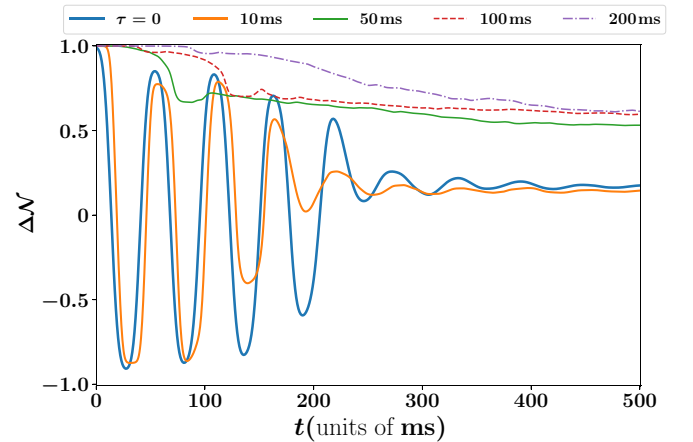


FIG. 10. Temporal evolution of the interwell population imbalance $\Delta\mathcal{N}(t)$ following a linear decrease of the energy offset from $D = 7 \hbar\omega_x/l_{\text{osc}}$ to $D = 0$ for different ramp rates τ (see legend). A larger ramp rate of the quench protocol leads progressively to tunneling suppression. The quasi-1D dBEC consists of $N = 40000$ ^{164}Dy atoms with $\epsilon_{\text{dd}} = 1.394$.

initial guess wave function. The choice of the initial ansatz is naturally more crucial in two dimensions due to the relatively higher degrees of freedom.

To identify the correct ground state, we evaluate the corresponding energies of different initial states with precision up to ten decimal digits. The normalization of the wave function at every step of the imaginary time evolution is preserved by applying $\psi(\mathbf{r}', t) \rightarrow N^{1/2}/|\psi(\mathbf{r}', t)|$. Convergence is justified by testifying that modifications of the wave function (at every grid point) between consecutive time steps is lower than 10^{-6} and the corresponding energy alterations lie below 10^{-8} . This serves as the initial state for the quench-induced tunneling dynamics which is monitored through real time propagation of the eGPE. The divergent behavior of the

dipolar interaction potential at short distances is circumvented by transforming to momentum space [83] for the calculations. Subsequently, we employ the inverse Fourier transform to find the real space configurations relying on the convolution theorem. For the present simulations a 3D box with a spatial grid ($n_x \times n_y \times n_z$) is used which refers to $(1024 \times 128 \times 128)$ in the quasi-1D case and $(512 \times 512 \times 128)$ for the quasi-2D geometry. The spatial discretization is $\delta x = \delta y = \delta z = 0.05 l_{\text{osc}}$, and the time step of the numerical integration $\delta t = 10^{-5}/\omega_x$. Hence, to accurately simulate the real time dynamics of the system we guarantee that $(\delta t)^2 < \delta x \delta y$ [82] is satisfied. Indeed, such spatial and time discretization steps ensure that the total particle number and total energy remain conserved, numerically of the order of 10^{-6} , during the evolution.

-
- [1] A. Griesmaier, J. Werner, S. Hensler, J. Stuhler, and T. Pfau, Bose-Einstein condensation of chromium, *Phys. Rev. Lett.* **94**, 160401 (2005).
- [2] M. Lu, N. Q. Burdick, S. H. Youn, and B. L. Lev, Strongly dipolar Bose-Einstein condensate of dysprosium, *Phys. Rev. Lett.* **107**, 190401 (2011).
- [3] K. Aikawa, A. Frisch, M. Mark, S. Baier, A. Rietzler, R. Grimm, and F. Ferlaino, Bose-Einstein condensation of erbium, *Phys. Rev. Lett.* **108**, 210401 (2012).
- [4] Y. Miyazawa, R. Inoue, H. Matsui, G. Nomura, and M. Kozuma, Bose-Einstein condensation of europium, *Phys. Rev. Lett.* **129**, 223401 (2022).
- [5] T. Lahaye, C. Menotti, L. Santos, M. Lewenstein, and T. Pfau, The physics of dipolar bosonic quantum gases, *Rep. Prog. Phys.* **72**, 126401 (2009).
- [6] F. Böttcher, J.-N. Schmidt, J. Hertkorn, K. S. H. Ng, S. D. Graham, M. Guo, T. Langen, and T. Pfau, New states of matter with fine-tuned interactions: quantum droplets and dipolar supersolids, *Rep. Prog. Phys.* **84**, 012403 (2021).
- [7] L. Chomaz, I. Ferrier-Barbut, F. Ferlaino, B. Laburthe-Tolra, B. L. Lev, and T. Pfau, Dipolar physics: A review of experiments with magnetic quantum gases, *Rep. Prog. Phys.* **86**, 026401 (2023).
- [8] H. Kadau, M. Schmitt, M. Wenzel, C. Wink, T. Maier, I. Ferrier-Barbut, and T. Pfau, Observing the Rosensweig instability of a quantum ferrofluid, *Nature (London)* **530**, 194 (2016).
- [9] I. Ferrier-Barbut, H. Kadau, M. Schmitt, M. Wenzel, and T. Pfau, Observation of quantum droplets in a strongly dipolar Bose gas, *Phys. Rev. Lett.* **116**, 215301 (2016).
- [10] L. Chomaz, S. Baier, D. Petter, M. J. Mark, F. Wächtler, L. Santos, and F. Ferlaino, Quantum-fluctuation-driven crossover from a dilute Bose-Einstein condensate to a macrodroplet in a dipolar quantum fluid, *Phys. Rev. X* **6**, 041039 (2016).
- [11] M. Schmitt, M. Wenzel, F. Böttcher, I. Ferrier-Barbut, and T. Pfau, Self-bound droplets of a dilute magnetic quantum liquid, *Nature (London)* **539**, 259 (2016).
- [12] F. Wächtler and L. Santos, Quantum filaments in dipolar Bose-Einstein condensates, *Phys. Rev. A* **93**, 061603(R) (2016).
- [13] F. Wächtler and L. Santos, Ground-state properties and elementary excitations of quantum droplets in dipolar Bose-Einstein condensates, *Phys. Rev. A* **94**, 043618 (2016).
- [14] N. Henkel, R. Nath, and T. Pohl, Three-dimensional roton excitations and supersolid formation in Rydberg-excited Bose-Einstein condensates, *Phys. Rev. Lett.* **104**, 195302 (2010).
- [15] F. Cinti, P. Jain, M. Boninsegni, A. Micheli, P. Zoller, and G. Pupillo, Supersolid droplet crystal in a dipole-blockaded gas, *Phys. Rev. Lett.* **105**, 135301 (2010).
- [16] J.-R. Li, J. Lee, W. Huang, S. Burchesky, B. Shteynas, F. C. Top, A. O. Jamison, and W. Ketterle, A stripe phase with supersolid properties in spin-orbit-coupled Bose-Einstein condensates, *Nature (London)* **543**, 91 (2017).
- [17] J. Léonard, A. Morales, P. Zupancic, T. Donner, and T. Esslinger, Monitoring and manipulating Higgs and Goldstone modes in a supersolid quantum gas, *Science* **358**, 1415 (2017).
- [18] J. Léonard, A. Morales, P. Zupancic, T. Esslinger, and T. Donner, Supersolid formation in a quantum gas breaking a continuous translational symmetry, *Nature (London)* **543**, 87 (2017).
- [19] F. Böttcher, J.-N. Schmidt, M. Wenzel, J. Hertkorn, M. Guo, T. Langen, and T. Pfau, Transient supersolid properties in an array of dipolar quantum droplets, *Phys. Rev. X* **9**, 011051 (2019).
- [20] L. Tanzi, E. Lucioni, F. Famà, J. Catani, A. Fioretti, C. Gabbanini, R. N. Bisset, L. Santos, and G. Modugno, Observation of a dipolar quantum gas with metastable supersolid properties, *Phys. Rev. Lett.* **122**, 130405 (2019).
- [21] L. Chomaz, D. Petter, P. Ilzhöfer, G. Natale, A. Trautmann, C. Politi, G. Durastante, R. M. W. van Bijnen, A. Patscheider, M. Sohmen, M. J. Mark, and F. Ferlaino, Long-lived and transient supersolid behaviors in dipolar quantum gases, *Phys. Rev. X* **9**, 021012 (2019).
- [22] D. S. Petrov, Quantum mechanical stabilization of a collapsing Bose-Bose mixture, *Phys. Rev. Lett.* **115**, 155302 (2015).
- [23] R. N. Bisset, R. M. Wilson, D. Baillie, and P. B. Blakie, Ground-state phase diagram of a dipolar condensate with quantum fluctuations, *Phys. Rev. A* **94**, 033619 (2016).
- [24] D. Baillie and P. B. Blakie, Droplet crystal ground states of a dipolar Bose gas, *Phys. Rev. Lett.* **121**, 195301 (2018).
- [25] T. D. Lee, K. Huang, and C. N. Yang, Eigenvalues and eigenfunctions of a Bose system of hard spheres and its low-temperature properties, *Phys. Rev.* **106**, 1135 (1957).
- [26] A. R. P. Lima and A. Pelster, Quantum fluctuations in dipolar Bose gases, *Phys. Rev. A* **84**, 041604(R) (2011).

- [27] M. A. Norcia, C. Politi, L. Klaus, E. Poli, M. Sohmen, M. J. Mark, R. N. Bisset, L. Santos, and F. Ferlaino, Two-dimensional supersolidity in a dipolar quantum gas, *Nature (London)* **596**, 357 (2021).
- [28] E. P. Gross, Unified theory of interacting bosons, *Phys. Rev.* **106**, 161 (1957).
- [29] E. P. Gross, Classical theory of boson wave fields, *Ann. Phys. (NY)* **4**, 57 (1958).
- [30] C. N. Yang, Concept of off-diagonal long-range order and the quantum phases of liquid He and of superconductors, *Rev. Mod. Phys.* **34**, 694 (1962).
- [31] A. F. Andreev and I. M. Lifshits, Quantum theory of defects in crystals, *Zh. Eksp. Teor. Fiz.* **56**, 2057 (1969) [*JETP* **29**, 1107 (1969)].
- [32] G. V. Chester, Speculations on Bose-Einstein condensation and quantum crystals, *Phys. Rev. A* **2**, 256 (1970).
- [33] A. J. Leggett, Can a solid be superfluid? *Phys. Rev. Lett.* **25**, 1543 (1970).
- [34] L. Chomaz, R. M. W. van Bijnen, D. Petter, G. Faraoni, S. Baier, J. H. Becher, M. J. Mark, F. Wächtler, L. Santos, and F. Ferlaino, Observation of roton mode population in a dipolar quantum gas, *Nat. Phys.* **14**, 442 (2018).
- [35] M. Guo, F. Böttcher, J. Hertkorn, J.-N. Schmidt, M. Wenzel, H. P. Büchler, T. Langen, and T. Pfau, The low-energy Goldstone mode in a trapped dipolar supersolid, *Nature (London)* **574**, 386 (2019).
- [36] G. Natale, R. M. W. van Bijnen, A. Patscheider, D. Petter, M. J. Mark, L. Chomaz, and F. Ferlaino, Excitation spectrum of a trapped dipolar supersolid and its experimental evidence, *Phys. Rev. Lett.* **123**, 050402 (2019).
- [37] L. Tanzi, S. M. Roccuzzo, E. Lucioni, F. Fama, A. Fioretti, C. Gabbanini, G. Modugno, A. Recati, and S. Stringari, Supersolid symmetry breaking from compressional oscillations in a dipolar quantum gas, *Nature (London)* **574**, 382 (2019).
- [38] E. Poli, T. Bland, C. Politi, L. Klaus, M. A. Norcia, F. Ferlaino, R. N. Bisset, and L. Santos, Maintaining supersolidity in one and two dimensions, *Phys. Rev. A* **104**, 063307 (2021).
- [39] T. Bland, E. Poli, C. Politi, L. Klaus, M. A. Norcia, F. Ferlaino, L. Santos, and R. N. Bisset, Two-dimensional supersolid formation in dipolar condensates, *Phys. Rev. Lett.* **128**, 195302 (2022).
- [40] Y.-C. Zhang, T. Pohl, and F. Maucher, Phases of supersolids in confined dipolar Bose-Einstein condensates, *Phys. Rev. A* **104**, 013310 (2021).
- [41] J. Hertkorn, J.-N. Schmidt, M. Guo, F. Böttcher, K. S. H. Ng, S. D. Graham, P. Uerlings, T. Langen, M. Zwierlein, and T. Pfau, Pattern formation in quantum ferrofluids: From supersolids to superglasses, *Phys. Rev. Res.* **3**, 033125 (2021).
- [42] M. Schmidt, L. Lassablière, G. Quémener, and T. Langen, Self-bound dipolar droplets and supersolids in molecular Bose-Einstein condensates, *Phys. Rev. Res.* **4**, 013235 (2022).
- [43] E. J. Halperin, S. Ronen, and J. L. Bohn, Frustration in a dipolar Bose-Einstein condensate introduced by an optical lattice, *Phys. Rev. A* **107**, L041301 (2023).
- [44] J. C. Smith, D. Baillie, and P. B. Blakie, Quantum droplet states of a binary magnetic gas, *Phys. Rev. Lett.* **126**, 025302 (2021).
- [45] S. Li, U. N. Le, and H. Saito, Long-lifetime supersolid in a two-component dipolar Bose-Einstein condensate, *Phys. Rev. A* **105**, L061302 (2022).
- [46] C. Politi, A. Trautmann, P. Ilzhöfer, G. Durastante, M. J. Mark, M. Modugno, and F. Ferlaino, Interspecies interactions in an ultracold dipolar mixture, *Phys. Rev. A* **105**, 023304 (2022).
- [47] D. Scheiermann, L. A. P. Ardila, T. Bland, R. N. Bisset, and L. Santos, Catalyzation of supersolidity in binary dipolar condensates, *Phys. Rev. A* **107**, L021302 (2023).
- [48] T. Bland, E. Poli, L. A. P. Ardila, L. Santos, F. Ferlaino, and R. N. Bisset, Alternating-domain supersolids in binary dipolar condensates, *Phys. Rev. A* **106**, 053322 (2022).
- [49] M. A. Norcia and F. Ferlaino, Developments in atomic control using ultracold magnetic lanthanides, *Nat. Phys.* **17**, 1349 (2021).
- [50] S. Halder, K. Mukherjee, S. I. Mistakidis, S. Das, P. G. Kevrekidis, P. K. Panigrahi, S. Majumder, and H. R. Sadeghpour, Control of ^{164}Dy Bose-Einstein condensate phases and dynamics with dipolar anisotropy, *Phys. Rev. Res.* **4**, 043124 (2022).
- [51] K. Mukherjee, M. N. Tengstrand, T. A. Cardinale, and S. M. Reimann, Supersolid stacks in antipolar Bose-Einstein condensates, *Phys. Rev. A* **108**, 023302 (2023).
- [52] F. Ancilotto, M. Barranco, M. Pi, and L. Reatto, Vortex properties in the extended supersolid phase of dipolar Bose-Einstein condensates, *Phys. Rev. A* **103**, 033314 (2021).
- [53] L. Klaus, T. Bland, E. Poli, C. Politi, G. Lamporesi, E. Casotti, R. N. Bisset, M. J. Mark, and F. Ferlaino, Observation of vortices and vortex stripes in a dipolar condensate, *Nat. Phys.* **18**, 1453 (2022).
- [54] T. Bland, G. Lamporesi, M. J. Mark, and F. Ferlaino, Vortices in dipolar Bose-Einstein condensates, *Comptes Rendus. Physique* **24**, 133 (2023).
- [55] M. N. Tengstrand, D. Boholm, R. Sachdeva, J. Bengtsson, and S. M. Reimann, Persistent currents in toroidal dipolar supersolids, *Phys. Rev. A* **103**, 013313 (2021).
- [56] M. Nilsson Tengstrand, P. Stürmer, J. Ribbing, and S. M. Reimann, Toroidal dipolar supersolid with a rotating weak link, *Phys. Rev. A* **107**, 063316 (2023).
- [57] M. Sohmen, C. Politi, L. Klaus, L. Chomaz, M. J. Mark, M. A. Norcia, and F. Ferlaino, Birth, life, and death of a dipolar supersolid, *Phys. Rev. Lett.* **126**, 233401 (2021).
- [58] J. Sánchez-Baena, C. Politi, F. Maucher, F. Ferlaino, and T. Pohl, Heating a dipolar quantum fluid into a solid, *Nat. Commun.* **14**, 1868 (2023).
- [59] R. Gati and M. K. Oberthaler, A bosonic Josephson junction, *J. Phys. B: At. Mol. Opt. Phys.* **40**, R61 (2007).
- [60] S. Keshavamurthy and P. Schlagheck, *Dynamical Tunneling: Theory and Experiment* (CRC Press, Boca Raton, FL, 2011).
- [61] B. D. Josephson, Possible new effects in superconductive tunnelling, *Phys. Lett.* **1**, 251 (1962).
- [62] M. Albiez, R. Gati, J. Fölling, S. Hunsmann, M. Cristiani, and M. K. Oberthaler, Direct observation of tunneling and nonlinear self-trapping in a single bosonic Josephson junction, *Phys. Rev. Lett.* **95**, 010402 (2005).
- [63] A. Smerzi, S. Fantoni, S. Giovanazzi, and S. R. Shenoy, Quantum coherent atomic tunneling between two trapped Bose-Einstein condensates, *Phys. Rev. Lett.* **79**, 4950 (1997).
- [64] S. Raghavan, A. Smerzi, S. Fantoni, and S. R. Shenoy, Coherent oscillations between two weakly coupled Bose-Einstein condensates: Josephson effects, π oscillations, and macroscopic quantum self-trapping, *Phys. Rev. A* **59**, 620 (1999).

- [65] S. I. Mistakidis, A. G. Volosniev, R. E. Barfknecht, T. Fogarty, Th. Busch, A. Foerster, P. Schmelcher, and N. T. Zinner, Few-body Bose gases in low dimensions- a laboratory for quantum dynamics, *Phys. Rep.* **1042**, 1 (2023).
- [66] T. Koch, T. Lahaye, J. Metz, B. Fröhlich, A. Griesmaier, and T. Pfau, Stabilization of a purely dipolar quantum gas against collapse, *Nat. Phys.* **4**, 218 (2008).
- [67] P. Ilzhöfer, M. Sohmen, G. Durastante, C. Politi, A. Trautmann, G. Natale, G. Morpurgo, T. Giamarchi, L. Chomaz, M. J. Mark, and F. Ferlaino, Phase coherence in out-of-equilibrium supersolid states of ultracold dipolar atoms, *Nat. Phys.* **17**, 356 (2021).
- [68] J. Crank and P. Nicolson, A practical method for numerical evaluation of solutions of partial differential equations of the heat-conduction type, *Math. Proc. Camb. Philos. Soc.* **43**, 50 (1947).
- [69] G. J. Milburn, J. Corney, E. M. Wright, and D. F. Walls, Quantum dynamics of an atomic Bose-Einstein condensate in a double-well potential, *Phys. Rev. A* **55**, 4318 (1997).
- [70] S. Levy, E. Lahoud, I. Shomroni, and J. Steinhauer, The ac and dc Josephson effects in a Bose-Einstein condensate, *Nature (London)* **449**, 579 (2007).
- [71] See this url for the dynamics of a quasi-1D SS subjected initially to a weak energy offset, <https://drive.google.com/drive/u/1/folders/1xaUq5tiL187U1qtb4Csc2oKLzx12zhS>.
- [72] K. Mukherjee and S. M. Reimann, Classical-linear-chain behavior from dipolar droplets to supersolids, *Phys. Rev. A* **107**, 043319 (2023).
- [73] S. Ronen, D. C. E. Bortolotti, and J. L. Bohn, Bogoliubov modes of a dipolar condensate in a cylindrical trap, *Phys. Rev. A* **74**, 013623 (2006).
- [74] See this url for tunneling suppression and vibrational modes of the SS crystals in a quasi-2D dBEC with an initially small energy offset, <https://drive.google.com/drive/u/1/folders/1qQwP0w-pqrYWZFyvc9Ls7OHBxaI4Qm5P>.
- [75] L. Cao, V. Bolsinger, S. I. Mistakidis, G. M. Koutentakis, S. Krönke, J. M. Schurer, and P. Schmelcher, A unified *ab initio* approach to the correlated quantum dynamics of ultracold fermionic and bosonic mixtures, *J. Chem. Phys.* **147**, 044106 (2017).
- [76] S. K. Haldar and O. E. Alon, Many-body quantum dynamics of a bosonic Josephson junction with a finite-range interaction, *J. Phys.: Conf. Ser.* **1206**, 012010 (2019).
- [77] P. Engels, C. Atherton, and M. A. Hofer, Observation of faraday waves in a Bose-Einstein condensate, *Phys. Rev. Lett.* **98**, 095301 (2007).
- [78] K. Kwon, K. Mukherjee, S. J. Huh, K. Kim, S. I. Mistakidis, D. K. Maity, P. G. Kevrekidis, S. Majumder, P. Schmelcher, and J.-y. Choi, Spontaneous formation of star-shaped surface patterns in a driven Bose-Einstein condensate, *Phys. Rev. Lett.* **127**, 113001 (2021).
- [79] T. Maier, H. Kadau, M. Schmitt, M. Wenzel, I. Ferrier-Barbut, T. Pfau, A. Frisch, S. Baier, K. Aikawa, L. Chomaz, M. J. Mark, F. Ferlaino, C. Makrides, E. Tiesinga, A. Petrov, and S. Kotochigova, Emergence of chaotic scattering in ultracold Er and Dy, *Phys. Rev. X* **5**, 041029 (2015).
- [80] R. N. Bisset and P. B. Blakie, Crystallization of a dilute atomic dipolar condensate, *Phys. Rev. A* **92**, 061603(R) (2015).
- [81] K.-T. Xi and H. Saito, Droplet formation in a Bose-Einstein condensate with strong dipole-dipole interaction, *Phys. Rev. A* **93**, 011604(R) (2016).
- [82] X. Antoine, W. Bao, and C. Besse, Computational methods for the dynamics of the nonlinear Schrödinger/Gross-Pitaevskii equations, *Comput. Phys. Commun.* **184**, 2621 (2013).
- [83] K. Góral and L. Santos, Ground state and elementary excitations of single and binary Bose-Einstein condensates of trapped dipolar gases, *Phys. Rev. A* **66**, 023613 (2002).